THE CUMULUS, PHOTOGRAMMETRIC, IN SITU, AND DOPPLER OBSERVATIONS EXPERIMENT OF 2006

BY R. DAMIANI, J. ZEHNDER, B. GEERTS, J. DEMKO, S. HAIMOV, J. PETTI, G. S. POULOS, A. RAZDAN, J. HU, M. LEUTHOLD, AND J. FRENCH

Detailed airborne and ground-based measurements, including radar and stereocamera data, were collected over an isolated mountain in Arizona to study the dynamics of cumulus clouds evolving from shallow to deep convection.
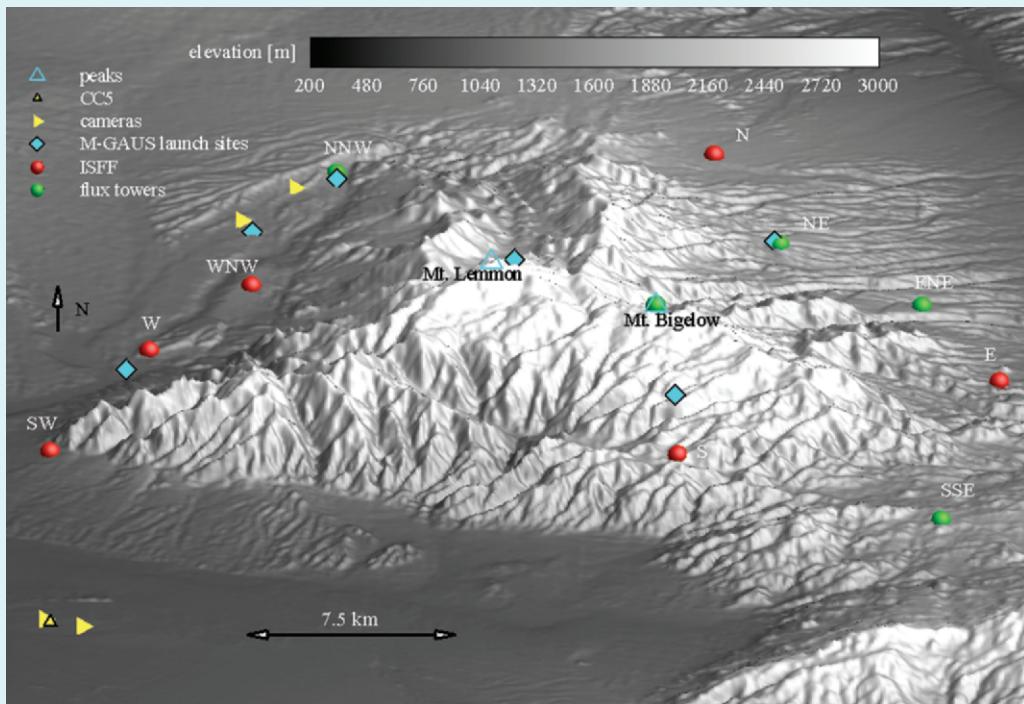
FIG. 1. Instrumentation layout around the Catalina Mountains. Tucson stretches across the plains in the lower left of the image. CC5 is the fifth camera, used for nowcasting. Labels next to integrated surface flux facility (ISFF) location symbols are the conventional station names in CuPIDO.

CuPIDO OBJECTIVES AND HYPOTHESES. Cumulus convection is the primary mechanism of boundary layer (BL)–trosphere exchange and precipitation in quasi-barotropic environments. It operates at a broad range of temporal and spatial scales. Mountain ranges over the western United States and elsewhere trigger warm-season cumulus convection with remarkable regularity. Sensible heat flux over isolated elevated terrain drives an upslope flow that may trigger and lock the initial deep convection in place. The "sky islands" (Coblentz and Riitters 2004) in the southwestern United States thus serve as ▶

natural laboratories for cumulus convection studies (Raymond and Wilkening 1982), because of their considerable elevation gain over the desert plains and their compact horizontal extent. The Cumulus Photogrammetric, In Situ, and Doppler Observations (CuPIDO) experiment was performed over one of these sky islands, benefiting from the regular timing and location of cumulus convection. It took place during the summer monsoon of 2006 over and around the Santa Catalina Mountains in southern Arizona. This mountain has a horizontal scale of ~20 km and a vertical scale of about 2100 m over the surrounding plains (Fig. 1).

Several observational studies in the desert Southwest have addressed orographic circulations and/or cumulus dynamics (Braham et al. 1951; Braham and Draginis 1960; Fujita et al. 1962; Todd 1964; Raymond and Wilkening 1980, 1982; Dye et al. 1989; Raymond and Blyth 1989; Blyth and Latham 1993). None achieved CuPIDO's in situ and remote data density and none studied the onset of the first cumulus. CuPIDO has yielded an unprecedented dataset to study both fundamental cumulus dynamics, and the synergy between mountain-scale BL circulations and orographic cumulus convection.

One aspect of the CuPIDO investigation relates to the thermally direct anabatic circulation over a heated mountain, and its possible transition from BL flow (e.g., Orville 1964) to deep convection. Net heating and moistening in the column of air above the mountain, resulting from detrainment by successive cumulus towers of BL air, which is high in equivalent potential temperature (θ_e), may indeed strengthen that circulation. However, Raymond and Wilkening (1982) find that the shallow orographic circulation is not altered much by the development of a thunderstorm.

AFFILIATIONS: Damiani, Geerts, Demko, Haimov, and French—University of Wyoming, Laramie, Wyoming; Zehnder, Razdan, and Hu—Arizona State University, Tempe, Arizona; Petti and Leuthold—University of Arizona, Tucson, Arizona; Poulos—NCAR, Boulder, Colorado
CORRESPONDING AUTHOR: Bart Geerts, Department of Atmospheric Sciences, University of Wyoming, Laramie, WY 82071
E-mail: geerts@uwyo.edu

A related question regards the impact of detraining cumulus eddies on subsequent cumulus turrets. Stepwise development of new turrets through the remnants of their predecessors has been observed during CuPIDO, as well as in previous studies (e.g., Roessner et al. 1990; Zehnder et al. 2006, 2007). Stepwise development can be either due to conditioning of the environment in which successive cumuli form ("environmental preconditioning"), to increased buoyancy of successive thermals feeding the cumuli (associated with diurnal trend of surface heat fluxes), or both. The latter can be assessed by surface station data and airborne measurements in the BL. The former relies on the following two conditions: first, successive cumulus development must occur in air modified by previous convection (Perry and Hobbs 1996), and thus, for orographic convection, winds must be weak at all levels. This condition, that is, that the cumulus regeneration time scale is short compared to the advective time scale, did apply in some cases in CuPIDO. Second, the reduced cumulus erosion by entrainment (resulting from ambient moistening) must dominate over the buoyancy reduction (resulting from ambient heating). This second condition will be assessed using aircraft and sounding data.

Historically, observational studies of cumulus dynamics have been hampered by the complex and finescale 3D structure and rapid evolution of cumuli, complicating the interpretation of cumulus evolution and cumulus–environment interaction by means of in situ data from a sequence of aircraft cloud penetrations (e.g., Braham et al. 1951; Raymond and Wilkening 1982; Hobbs and Rangno 1985; Blythe and Latham 1993). Previous studies have also been hampered by poor knowledge of the cloud-base heights and the ambient stability and shear. In CuPIDO we use an airborne cloud radar configuration to provide a more complete spatial view of cumulus dynamics. Consecutive radar transects more readily reveal cumulus evolution and allow in situ data to be interpreted in that context. CuPIDO had the further benefit of regular radiosonde releases and photogrammetric data.

Boundary layer processes are tightly coupled with cumulus development, in particular over mountains. Real-time nested Weather Research and Forecasting (WRF) model simulations, with an inner grid resolution of 1.2 km, were conducted during the field phase. This effort confirmed the difficulty in predicting the timing and intensity of orographic convection. We believe that this challenge mainly lies in the parameterization of BL processes. CuPIDO data will be useful both in improving BL schemes in complex

terrain and in testing cumulus parameterizations in numerical weather prediction (NWP) and general circulation models.

CuPIDO was designed to test three fundamental hypotheses:

1) *The onset of convection results from elevated heating, low-level convergence over the mountain, and local BL deepening to the level of free convection (LFC).* Surface sensible heating over a mountain, starting shortly after sunrise, leads to an elevated BL. This results in a hydrostatic pressure gradient toward the mountain, which drives upslope flow accompanied by moisture convergence. Boundary layer thermals are thus advected toward the mountaintop and gradually increase in depth, eventually reaching the LFC. Therefore, the timing of the onset of convection is affected not only by atmospheric factors (static stability), but also factors affecting the surface energy balance (cloud cover and soil moisture).

2) *Subsequent convective development is affected by the mutual interaction between cumulus and the environment (environmental preconditioning).* The extent and mode in which the conditioning of the column occurs depend on the ambient thermodynamic and wind profile. During early cumulonimbus development, the upslope flow and moisture convergence may be enhanced by buoyancy-induced pressure reduction near the LFC. As deep convection matures and a cold pool develops in the boundary layer, the upslope flow may be temporarily blocked on the downwind side of the mountain. This dynamic synergy between towering cumulus convection and the mountain-scale toroidal circulation determines the time scale of subsequent convective development.

3) *The main growth mechanism of cumulus turrets consists of a succession of thermals containing cloud-scale toroidal circulations, which govern both entrainment and cloud microphysical processes.* The pulsating nature of convective clouds, combined with toroidal circulations active in the ascending tops (Damiani et al. 2006), impact entrainment processes, hydrometeor recycling, aerosol evolution, drop size distribution, and precipitation development. The toroidal motion can also affect the rise of the thermals by opposing the horizontal pressure gradient force resulting from the interaction between an updraft and the ambient vertical wind shear, thus favoring the deepening of the cloud (Damiani and Vali 2007).

CuPIDO EXPERIMENTAL DESIGN AND RATIONALE.
Testing the hypotheses listed above requires both accurate monitoring of temperature, moisture, and wind in the BL and aloft, and depictions of cloud entrainment/detrainment and flow motions. CuPIDO was conducted over the Santa Catalina Mountains during the North American monsoon season. A network of surface meteorology stations and digital cameras was operated from 1 July through 31 August 2006. In addition, aircraft and sounding data were collected during 15 intensive operation periods (IOPs) between 18 July and 17 August.

In southern Arizona a generally dry condition during the spring and early summer, associated with prevailing midlatitude westerlies aloft, transitions to deep southeasterly or southerly winds that transport moisture from the Gulf of Mexico and the tropical eastern North Pacific (e.g., Bryson and Lowry 1955; Hales 1974). The increase in low-level water vapor enables the formation of deep convection characteristic of the North American monsoon (Adams and Comrie 1997).

Typical monsoonal convection has a distinct diurnal cycle, with clear skies before dawn and shallow convection beginning at about 0900 Mountain Standard Time (MST), with an eventual transition to cumulonimbus by about noon. Typically, a deep mixed BL develops with little capping, limited convective available potential energy (CAPE), typically below 1500 J kg^{-1}, and a dry midtroposphere, so that the convection develops slowly and in stages. Such typical monsoon days were targeted in CuPIDO, although conditions can vary considerably from day to day. An occasional westerly trough in the upper-tropospheric flow can result in mid- and low-level drying and a break in the monsoon. There are also periodic intrusions of low-level moisture from the Gulf of California, referred to as gulf surges (e.g., Hales 1972), that may cause heavy precipitation.

Observing platforms and operations. Ground-based observations relied on two stereopairs of digital cameras, and a network of weather stations deployed around the Santa Catalina Mountains near Tucson. Figure 1 shows the location of the cameras and the "Sterophotogrammetric analysis" sidebar describes the principal of stereophotogrammetry. Ten ISFF stations, all measuring meteorological variables at 5-min intervals, were located around the base of the mountain (Fig. 1). Four of them were equipped with sonic anemometers and ultraviolet absorption

hygrometers for surface latent and sensible heat flux measurements. In addition, one station (labeled SSE on Fig. 1; photo in Fig. 2a) had a Licor 7500 for CO_2 flux measurements. (Information on the surface stations can be found online at www.eol.ucar.edu/rtf/projects/CUPIDO06/isff/ and www.sahra.arizona.edu/research/TAI/towers/tower_30mEC.html.) Additional flux measurements were recorded by the University of Arizona (UA) eddy correlation tower on Mt. Bigelow (Fig. 2b).

During the IOPs, the Mobile GPS Advanced Upper-Air Sounding System (MGAUS) soundings were released from various locations within the Santa Catalina Mountains, depending on prevailing
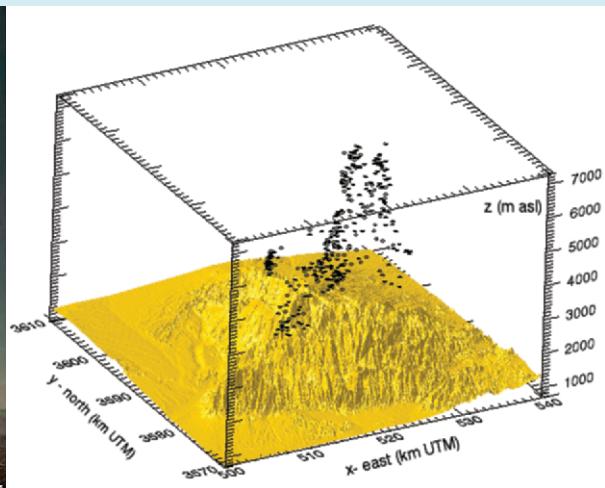
STEREO PHOTOGRAMMETRIC ANALYSIS

A novel aspect of CuPIDO is the operation of two pairs of digital cameras that are used to determine quantitative information on cumulus structure and evolution. The cameras used are standard CMOS-based IQinvision IQEYE303 Web cameras designed primarily for security purposes. The cameras accept a variety of lenses, and an 8-mm f1.5 lens provides a balance between maximum field of view with minimum barrel distortion.

Stereopairs were located both southwest and northwest of the mountains (see Fig. 1). The cameras were collocated with Apple Mac minicomputers used as ftp servers. JPEG images were transferred every 10 s during daylight hours to the server, with the transfer being controlled automatically by the cameras. Stereoanalysis is performed by locating the same cloud element on the pair of images and triangulating. This is done by defining a coordinate transformation between the image plane and 3D geocoordinates defined in terms of the intrinsic (pixel size and focal length) and extrinsic (position, elevation, and azimuth and roll angles) camera parameters. The 3D position of selected points on the frame determines the cumulus spatial structure from one vantage point, as shown on the right. Details on the stereo analysis technique are given in Zehnder et al. (2007). A fifth camera was located on the UA campus and was used for generating real-time, time-lapse movies that were used for operational purposes. These movies can be found in the CuPIDO archive (online at www.eol.ucar.edu/projects/cupido/).

Camera	IQeye303
Sensor	1/2″ optical format 3.15 megapixel CMOS, progressive scan with dichroic mirror
Pixels	2048 (H) × 1536 (V)
Storage	External network storage
Lens	Computar M0814-MP
Focal length	f = 8 mm F1.4
Field of view	52°

Typical image of cumuli over the Catalina Mountains, and stereo retrieval of cloud edges.

winds. Two MGAUS units, both using Vaisala RS-92 GPS-based radiosondes [information on the National Center for Atmospheric Research (NCAR) is online at www.eol.ucar.edu/facilities/gaus.html], were deployed, sometimes to different locations (launching at 60–90-min intervals) in other IOPs at the same site, resulting in 30–45-min interval soundings. Locations of the MGAUS launch sites are shown in Fig. 1.

The airborne platform was the University of Wyoming King Air (WKA), with a gust probe, an array of cloud particle probes, and high-frequency humidity and temperature sensors (for more details on WKA, see http://flights.uwyo.edu/base/InstList.pdf). In addition, the Wyoming Cloud Radar (WCR) operated on the WKA multi-Doppler configuration (see the "Wyoming Cloud Radar" sidebar).

Forecast guidance for field operations was provided by various operational models and the high-resolution WRF modeling system (version 2.1.2; see www.wrf-modeling.org/ for details) runs performed at UA. The nested domains had resolutions of 7.2 and 1.8 km. The Noah land surface model and the Mellor–Yamada–Janjic turbulent kinetic energy boundary layer scheme were used. Convection was explicitly modeled. IOP plans made on the previous day would be reassessed just after sunrise, based on visual observations, satellite and radar reflectivity imagery, output from the 0600 UTC WRF run, and the 1200 UTC Tucson (TUS) sounding. WKA and MGAUS operations were monitored in real time from an operations center at UA. Communications between the operation center and field units were possible through a dedicated xchat (online at www.xchat.org) channel provided by the NCAR/ Earth Observing Laboratory (EOL). Operations were assisted by real-time TUS operational radar data, National Lightning Detector Network (NLDN; online at www.unidata.ucar.edu/data/lightning.html) data, CC5 camera imagery (Fig. 1), and MGAUS soundings, all of which are viewable in an NCAR EOL-supported field catalog (see http://catalog.eol.ucar.edu/cupido/).

Key WKA data were transmitted to the ground using a low-bandwidth sat-ellite phone connection. These data were plotted in real time on top of radar and satellite imagery at the operations center, using the Integrated Data Viewer (IDV; online at www.unidata.ucar.edu.idv).

King Air flight strategies. Unlike in previous orographic cumulus experiments, the target WKA takeoff time in CuPIDO was *before* the appearance of the first cumulus, and was aimed to capture most of the cumulus evolution, specifically the transition from shallow to deep convection. Table 1 shows the IOP dates and flight times. On 6 out of a total of 15 IOPs, the WKA was airborne before the first cumulus developed over the mountain. The first orographic cumulus appeared within 60 min of takeoff on 10 IOPs. Optimal conditions called for fairly unstable soundings, with light winds aloft. These conditions would favor localized convection cycles. On many days, there was some capping present at roughly 450–500 hPa, often just above a layer of altostratus. While this is unusual for Arizona in summer, the capping inversion served to decelerate the growth of successive towers and allowed the aircraft to climb in unison with the main ascending turrets. On a few occasions, convection developed unusually quickly and the mission had to be aborted. The mission strategy and the flight patterns focused on one of the following three fundamental objectives: 1) cumulus dynamics, 2) BL dynamics, or 3) environmental modification by convection. In reality, most flights addressed multiple objectives (Table 1).

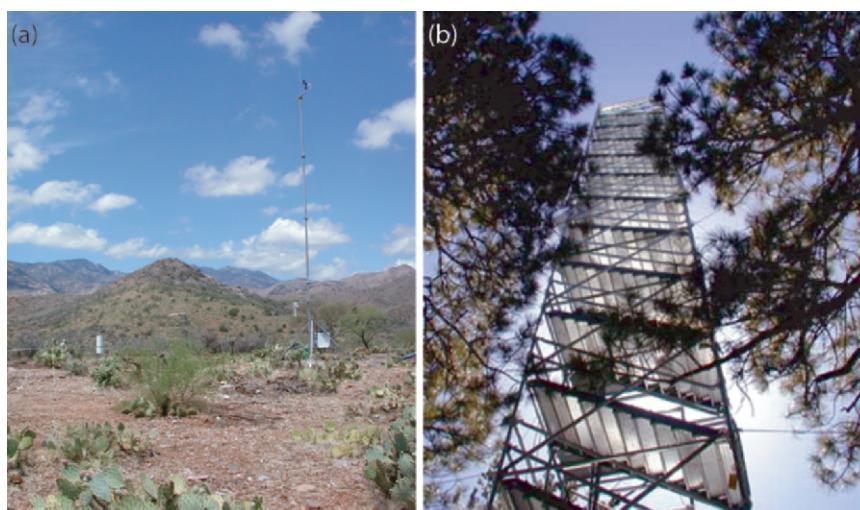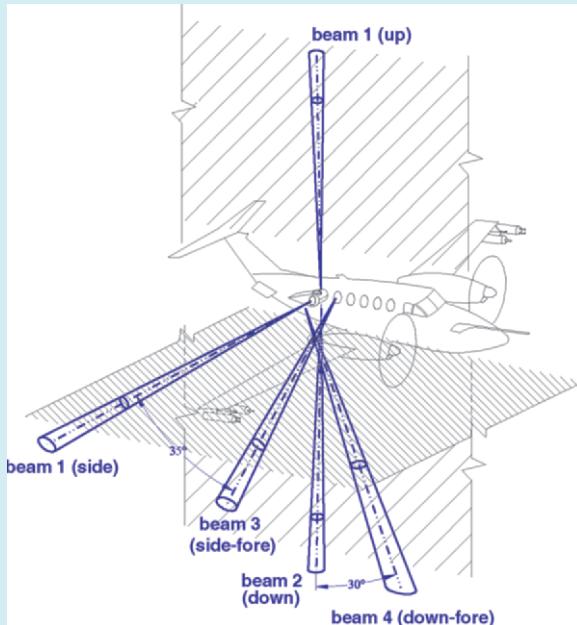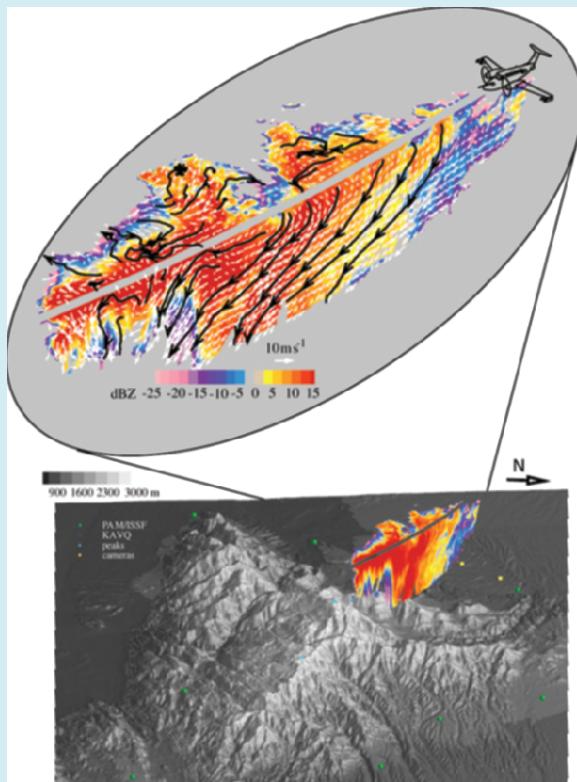Short-leg rosettes, racetrack patterns, and 90°–270° repeated traverses were flown for *cumulus*

Fɪɢ. 2. (a) One of the ISFF sites and (b) the Sustainability of Semi-Arid Hydrology and Riparian Areas (SAHARA) meteorological tower in pine forest on Mount Bigelow. All of the ISFF sites were in a semiarid environment, with little vegetation.

WYOMING CLOUD RADAR

The WCR (online at http://atmos.uwyo.edu/wcr) was a central instrument in CuPIDO, because its high-resolution reflectivity and multi-Doppler data revealed fine details of cumulus structure and kinematics. The WCR is quite sensitive (the minimum detectable signal is in the order of –27 dBZ at 1 km), yet CuPIDO has shown that shallow, warm cumuli (Fig. 13) and the optically clear BL (Fig. 10) are only marginally detectable.

WCR Configuration aboard the Wyoming King Air

WCR parameters.	
Transmit frequency	94.92 GHz
Peak power/duty cycle	1.6 KW / 1%
4 fixed antennas:	Aperture / beamwidth / polarization
• side/up	0.31 m / 0.7° / H, V
• side-force	0.31 m / 0.7° / single, linear
• down	0.46 m / 0.5° / single, linear
• down-fore	0.38 m / 0.6° / single, linear
Antenna modes (typical):	Beams (see image on the left):
• DPDD	1,2,3,4
• HBDD or HBDD+down	1,3 or 1,3 + 2
• profiling or profiling+side	1,2 or 1,2 + 3
• VPDD or up/side+VPDD	2,4 or 1 + 2,4
• profiling	1,2
Receiver channels:	2
• receiver outputs:	mag: log; phase: linear
• receiver dynamic range	> 70 dB
Dwell time/ along track sampling	30 ms / 3 – 5 m (typical)
Min. detectable signal (side antenna)	–37 dBZ @ 1km, 250ns, 500 avg
Resolution:	
• range	15 – 75 m
• volume @ 1 km, 250 ns pulse	37 × 12 × 15 m
Doppler velocity processor:	
• pulse pair	1st & 2nd moments
• fft spectrum	32 or 64 bins
Doppler Nyquist interval	±15.8 m/s^{-1}

Dual-plane dual-Doppler analysis of cumulus congestus over the Catalina Mountains

The WCR is a 95-GHz polarimetric Doppler radar installed primarily on the WKA. The WKA/WCR configuration includes four fixed antennas (see figure and table above) that allow horizontal and/or vertical scans of the clouds along the flight track. The two side- and two down-pointing beams can be used to perform HBDD and VPDD syntheses, rendering high-resolution 2D cloud kinematics to the side of or below the aircraft (Damiani and Haimov 2006; Leon et al. 2006). The side-pointing beam can also be redirected upward using a reflector plate housed in a fairing outside the cabin. The operational modes allow virtually simultaneous sampling of any combination of the four antennas. Two channels are sampled simultaneously; additional channels are sampled through an electronic switch. In most cases fewer than four antennas were used, in order to maximize sensitivity. The figure on the left shows an example of dual-plate dual-Doppler (DPDD) synthesis (reflectivity in color, and hydrometeor velocity as white vectors and selected black streamlines) from data collected in a precipitating cumulus congestus to the north of Mount Lemmon, 17 Aug 2006 at 1755 UTC. The flight level was 7450 m above sea level (ASL).

Table 1. CuPIDO IOP summary. In the second column (objectives) "1" refers to dynamics, "2" to BL dynamics, and "3" to environmental modification by convection. CAPE, CIN, and mean wind are computed from the MGAUS sounding nearest to the middle of the WKA flight. The mean wind is computed in the 700–500-hPa layer and is listed as speed@direction. The time of the first cumulus is derived from the CC5 time-lapse movies (Fig. 1). The number of loops refers to WKA mountain circumnavigations (Fig. 4). The extreme vertical velocities encountered by the WKA in cumuli are listed as w_{max}/w_{min}. The times listed are in UTC.

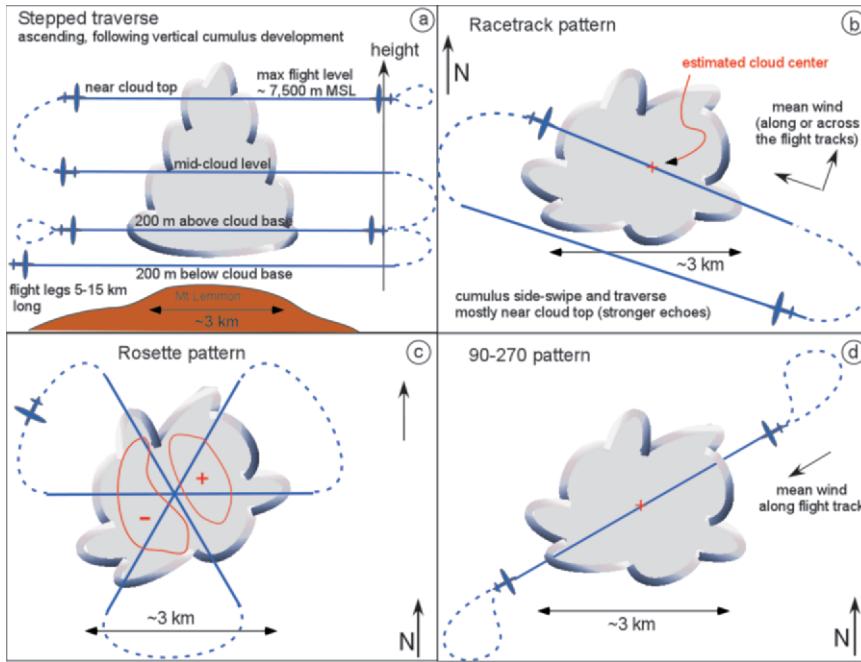| IOP	Date/time	Objectives	MGAUS locations (Fig. 1): times	CAPE CIN (J kg⁻¹)	Mean wind (m s⁻¹)	Time of first cumulus	No. of loops per soundings	No. of towers targeted per No. of cloud penetration	w_{max}/w_{min} (m s⁻¹) times of first anvil/ lightning
0	18 Jul 1614–1949	1, 3, 2	South-southeast: 1700	1020 / <5	8@143	1614	2 / 1	9 / 19	15/–10 / 2100 advected from the southeast/no
1	19 Jul 1600–2008	2	Windy Point: 1530, 1515, 1700, 1745, 1830, 1915, 2000	535 / 25	<2 m s⁻¹	1840	11 / 7	1/2	10/–6 / 2245/no
2	24 Jul 1600–2023	1, 3, 2	Northeast: 1600, 1645, 1730, 1815	110 / 115	6@64	1617	2 / 4	21 / 54	12/–9 / No/no
3	25 Jul 1556–2019	1, 2	Northeast; 1600, 1645, 1730, 1815, 1900, 1945	1560 / 50	4@41	1730	6 / 6	1 / 8	20/–9 / ?/?
4	26 Jul 1630–2008	2, 1, 3	Windy Point: 1600, 1645, 1730, 1815, 1900, 1945	1040 / 50	<2 m s⁻¹	1540	5 / 6	6 / 12	7/–5 / No/no
5	31 Jul 2019–0043	1, 3, 2	North-northwest: 2100, 2230	440 / <5	8@312	preexisting	1 / 2	19 / 62	12/–8 / No/no
6	1 Aug 1704–2011	1, 3	West: 1700, 1830 Windy Point: 1830	320 / 5	7@222	preexisting	2 / 3	30 traverses through one cluster	12/–9 / No/no
7	2 Aug 1616–2059	1, 2, 3	Windy Point and Mount Lemmon: 1600, 1730, 1900	270 / 0	4@204	1350	2 / 6	19 / 50	20/–17 / No/no
8	6 Aug 1756–2207	2, 1	Northeast: 1800, 1845, 1930, 2015, 2100	420 / 15	3@102	1805	8 / 4	1 / 18	18/–14 / No/no
9	7 Aug 1729–1901	1, 3, 2	Windy Point: 1730, 1800, 1830, 1930	715 / 10	5@161	1650	2 / 4	1 / 3	13/–6 / 1850/1854
10	8 Aug 1559–2037	2, 1, 3	Windy Point: 1530, 1600, 1630, 1700, 1730, 1800, 1830, 1900, 1930	890 / 45	4@97	1605	1 / 9	2–3 turrets along ridge / 43	19/–9 / 2036 advected from the east/no
11	9 Aug 1627–2258	3, 1	Windy Point: 1530, 1630, 1730, 1830, 1930; Northwest: 1730, 1830, 1930	830 / 120	6@133	1556	1 / 6	16 / 39	18/–10 / 1855/2040
12	10 Aug 1556–2040	1, 3, 2	Windy Point: 1530, 1630, 1700, 1730, 1800, 1830, 1900, 1930	1275 / 20	2@204	1515	2 / 8	17 / 47	25/–12 / 1730 and 1829/1830
13	11 Aug 1624–1830	3, 2	Windy Point: 1530, 1630, 1700, 1800, 1830, 1900, 1930	920 / 10	3@127	1454	3 / 6	3 boxes around deep convection	15/–6 / 1630/1630
14	13 Aug 1558–1820	3, 1	Mount Lemmon and West: 1530, 1630, 1730	2030 / 25	2@64	1330	1 / 6	8 passes at deep convection	17/–8 / Yes hidden by strata/1710
15	17 Aug 1552–1944	1, 3, 2	Mount Lemmon and Windy Point: 1530, 1630, 1730, 1830,1930	510 / 10	3@173	1425	2 / 10	11 / 39	19/–15 / 1800/1800

FIG. 3. Flight patterns used for cumulus dynamics studies.

the WCR; these cumuli were penetrated near cloud case with the WCR in profiling mode ("Wyoming Cloud Radar" sidebar). As the cumulus complex deepened, we tried to fly through or just above the tops of ascending towers, but only managed to do so on occasion.

To study *orographic BL dynamics*, some 50 low-level loops around the mountain were flown at various stages, mostly before the first orographic cumulus appearance (Fig. 4). Primarily two circumnavigation tracks were flown—one track mainly at ~310 m AGL over the ISFF stations, and a smaller

dynamics studies (Fig. 3). The rosettes were intended to maximize in-cloud flight time and were mainly aimed at measuring drop-size distributions, liquid water content, ice properties, and thermodynamic variables. The other flight patterns were conducted mainly for WCR measurements of cumulus temporal evolution. They were generally conducted along the main wind direction, and alternating WCR antenna modes (see "Wyoming Cloud Radar" sidebar) were used in order to collocate echo and kinematic features in two geometrical planes. Young, shallow cumuli were only marginally detectible by

loop (at ~500 m AGL) some 3.6 km closer to Mount Lemmon (Fig. 4). The WKA strayed very little from the location and altitude of these loops, so data from all 50 loops can be compared. The WCR was operated during most loops in order to characterize the BL depth and structure. Loop data can be used to estimate the horizontal convergence of mass, water vapor, and heat in the area contained within the loop, following a method similar to that used by Raymond and Wilkening (1982). The method uses the divergence theorem, which states that the line integral of the flow normal to a closed loop equals
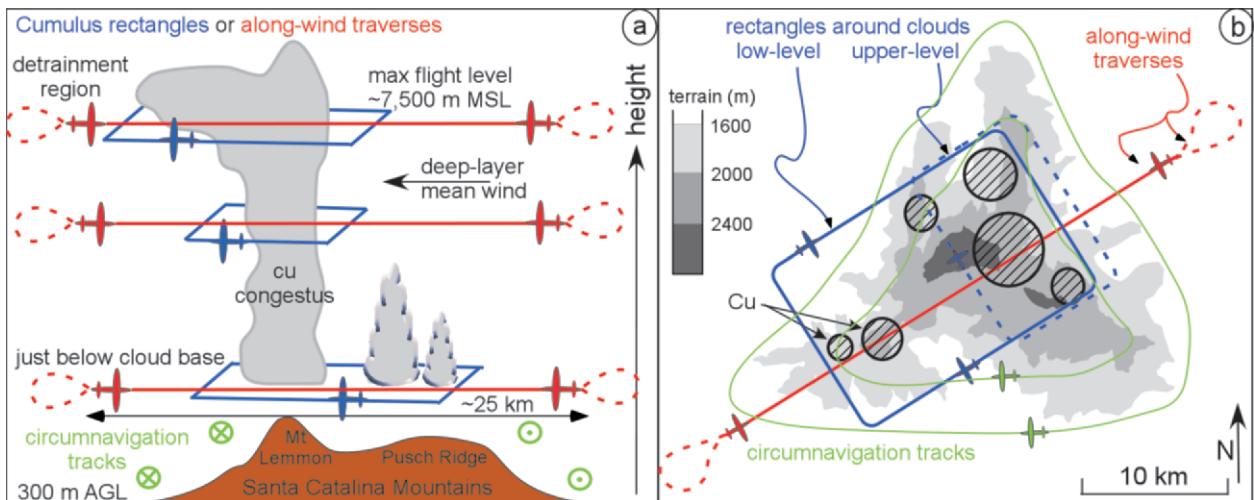

FIG. 4. Flight patterns used for BL dynamics and detrainment studies.

the mean convergence within the loop times the area of the loop.

Finally, to study *environmental modification by convection*, we performed mountain circumnavigations below cloud-base, wind-aligned 90°–270° tracks, and box patterns around clouds at various levels (Fig. 4). Above cloud base these tracks are used to determine the spatial patterns of detrainment, both in terms of range downwind from the cumulus, and in terms of azimuth relative to the mean wind direction.

CuPIDO CHALLENGES. Carrying out an observational field campaign in a harsh and remote environment such as the Sonoran Desert brings along a number of challenges. The ISFF stations needed to be located close to the mountain to capture the orographic circulations. Many of the ISFF locations were difficult to access, especially after the heavy rains encountered in late July (Fig. 5). Despite the difficulties, all ground stations worked well, with only two stations (north and northeast) being down briefly following lightning strikes during the second half of the campaign. Balloon staff had to be deployed hours in advance to allow for the drive to a suitably

upstream launch location, and had to be on site, in the desert, for the duration of the IOP. High air temperatures were a challenge both for the instrumentation and the personnel. The WCR transmitter often came close to overheating, especially during low-level mountain loops, and had to be shut down on occasion. Special procedures had to be devised to minimize the heat exhaust of the WCR in the WKA cabin.

Precise nowcasting was needed to pinpoint the optimal takeoff time (just before the first orographic cumulus) and the time of the first lightning, at which time WKA cloud penetrations had to be terminated. This proved to be quite difficult, and WRF soundings from the 0600 UTC run were of limited value. First cumulus nowcasting was based on the convective deficit criterion described by Zehnder et al. (2006), with the 1200 UTC TUS sounding as input and on occasion an early MGAUS sounding. This was complicated by the development of altostratus, usually just below the recurrent 450–500-hPa stable layer (e.g., Fig. 6). Too late a takeoff could mean missing the transition from shallow to deep convection, or ending up aborting the mission because of rapid cumulus electrification. Because the WKA endurance is just
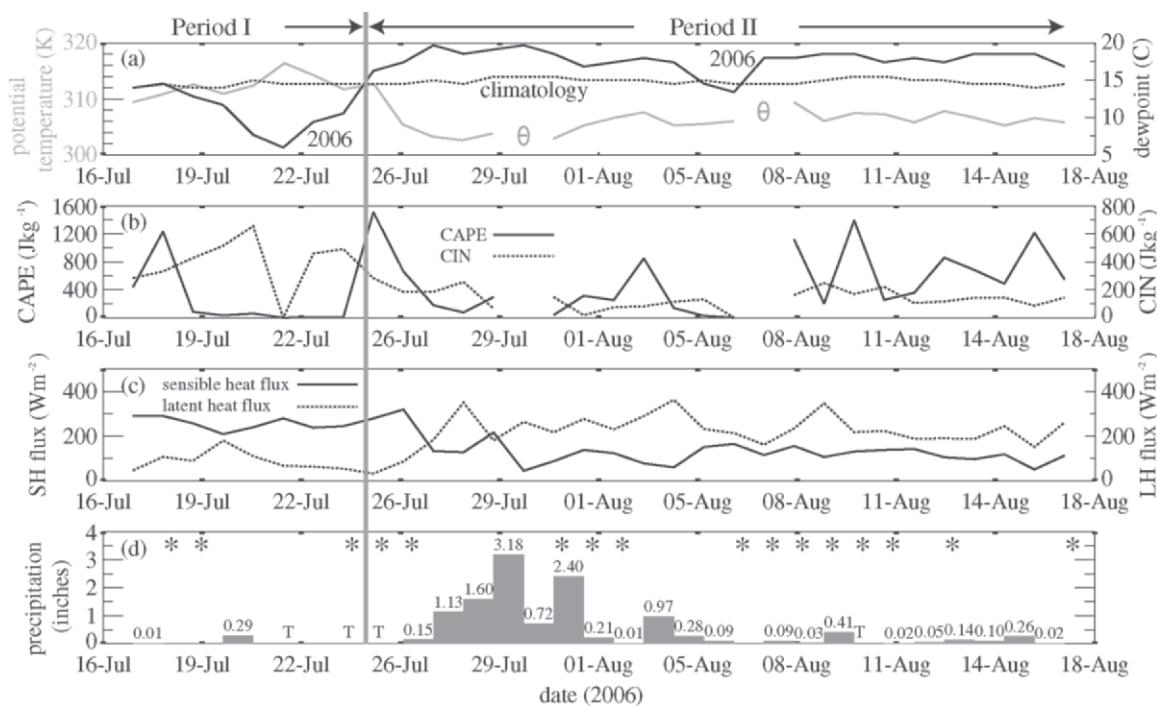

FIG. 5. Changes in atmospheric conditions during CuPIDO: (a) mean potential temperature of the lowest 500 m for the 1200 UTC TUS sounding (gray), and daily mean surface dewpoint (solid) and its climatology (dashed) at TUS; (b) CAPE and convective inhibition (CIN) for the same sounding; (c) peak latent heat (LH) and sensible heat (SH) flux (both averages for the four ISFF flux stations and a 30-min period); and (d) 24-h precipitation (average of 10 ISFF stations, T means trace or <0.01) and IOP days (stars). Breaks denote missing data. The two regimes are indicated as periods I and II.
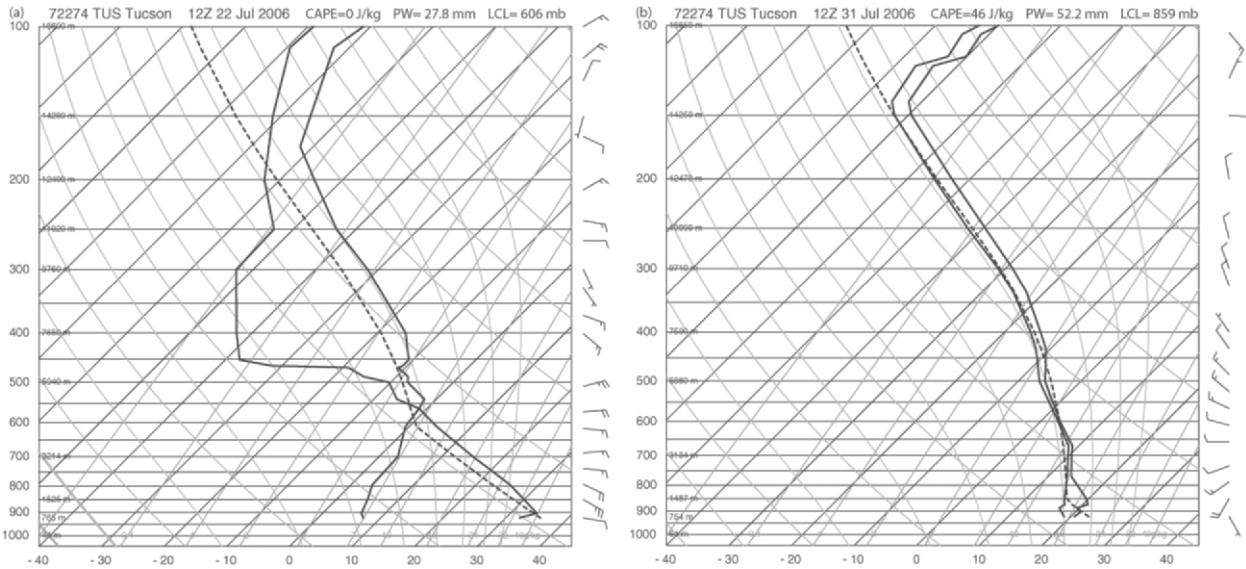
Fɪɢ. 6. Typical soundings during (a) period I and (b) period II.

4.5 h, an overly early start could result in missing most of the convection deepening cycles.

Coordinating flight patterns safely was perhaps the most difficult aspect of this project. The crew had to sustain strong vertical drafts, some exceeding 25 m s^{-1} (Table 1), resulting in airplane accelerations ranging between –1 and +2.5 G. The scientists in the operations center used xchat to relay information regarding thunderstorm activity and lightning flashes, based on both camera imagery and data from Next-Generation Weather Radar (NEXRAD) and NLDN displays. The MGAUS crews reported audible thunder. The WKA storm scope was also a great aid in keeping the aircraft away from lightning hazards. Within deep convection, ice riming on the control surfaces became a problem and limited aircraft performance.

CuPIDO has taught us a number of lessons on executing successful mission in safety. The first two lessons below apply to any field campaign with coordinated aircraft ground operations. The last three deal with cumulus studies.

- Real-time verbal communication via xchat was a considerable aid to operations, but an image can be worth a thousand words, and the aircrew would have benefited from the IDV-generated imagery itself, rather than the verbal descriptions based on that imagery. Low communication bandwidth did not allow us to effectively run IDV or browse Web pages in flight, thus, imagery needs to be transferred automatically during idle times.

- Real-time ISFF and MGAUS data are desirable. (The necessary communication was not cost effective in CuPIDO.) Aerological diagram images of completed MGAUS soundings were transmitted. They revealed changes in the BL and in stable layers and thus were useful to decision making. But, the 30-min delay to complete a sounding is large. Scientists should work with the ISFF/MGAUS crew in advance, to fine-tune real-time displays to be used for field guidance.

- Given the unpredictability of convective growth, we learned to be flexible about scientific objectives in flight. For instance, a break in the cloud growth during a cumulus dynamics mission allowed us to conduct box patterns at the detrainment level(s) and record changes in the environment.

- The climbing performance of the WKA deteriorates above 5500 m ASL, and the WKA could not climb as fast as some towering cumuli, thus compromising the CuPIDO cumulus dynamics objectives (Fig. 3). Also, desired flight clearances may be slow to obtain when air traffic control is busy. For these two reasons it is advisable to anticipate the cloud-top ascent and to loiter while cloud tops rise from below, relying mostly on WCR data at first. Updrafts at the upper levels resembled compact thermals, and not long-lasting plumes. As can also be seen in the time-lapse movies (see "Stereophotogrammetric Analysis" sidebar), cloud tops often display impressive rising bursts, followed by an equally fast collapse.

- Cumulus clouds evolve rapidly and often develop into clusters. Thus, visual identification of the

same target in successive passes was difficult. The onboard pointer instrument, tracking the estimated center of a turret, and the real-time track visualization only partially alleviated the problem. The difference in the time scales associated with cumulus growth and airplane maneuverability makes cumulus dynamics studies particularly complex. This problem can be alleviated with an airborne cloud radar.

PRELIMINARY FINDINGS. *Summary of IOPs.* Table 1 provides a summary of the CuPIDO IOPs. Cumulus dynamics missions were reserved for days with light wind and significant CAPE, supporting vigorous growth of individual towers. This type of study was often combined with the analysis of detrainment in the midtroposphere. On some flights, we conducted more than 40 penetrations into growing cumuli (IOPs 2, 5, 7, 10). Other missions, such as IOPs 1 and 8, focused on orographic BL dynamics, and WKA mostly circumnavigated the mountain at low levels.

Flights had to be suspended during two 4-day periods (Fig. 5); the first one on 20–23 July, because it was too dry, and the second one on 27–30 July, because it was too wet. Overcast morning skies, a record-moist sounding (e.g., Fig. 6b), and record precipitation occurred during the latter period. This was the result of a low-level moisture surge and upper-level northerly flow associated with a weak, quasistationary low over New Mexico. On three consecutive days the northerly flow aloft drove mesoscale convective systems (MCSs) southward during the late evening and at night. The MCSs were sustained by the large water vapor content in the BL (over 15 g kg^{-1}) and northerly low-level shear. Such flood-producing nocturnal MCSs are rare (McCollum et al. 1995) and were not predicted by operational models. In structure and predictability, these events are reminiscent of eastward-propagating nocturnal convection over the Great Plains (Carbone et al. 2002). Two ISFF stations (NE and ENE in Fig. 1) were severely damaged by the storms of that period.

The National Weather Service defines the Arizona monsoon period based on the daily mean dewpoint, which needs to exceed 12.2°C (54°F) for three consecutive days. Based on this definition, it began on 28 June 2006, nearly a week prior to the climatological onset. After the onset, conditions mostly remained moist in July and August, with only one break during the CuPIDO core phase (Fig. 5). Two periods can be distinguished during this phase. Period I (17–25 July) was marked by an anomalously low dewpoint and

high temperature (Fig. 5a), relatively high convective inhibition (Fig. 5b), and thus almost no rainfall (Fig 5d). The soil was dry and thus the surface latent heat flux was small compared to the sensible heat flux (Fig. 5c). This period had a relatively dry midtroposphere, so it is most suited to study cumulus detrainment and environmental preconditioning. The high sensible heat flux resulted in a relatively deep BL and strong mass convergence over the mountain. Period II, starting on 26 July, started with a moisture surge and moist tropical soundings (low CAPE, low CIN), as illustrated in Fig. 6b. The low-level humidity was so high that on occasion the LCL was *below* Mount Lemmon. Record-setting rainfall occurred around the Catalina Mountains (Fig. 5d), mainly from above-mentioned nocturnal MCSs, resulting in saturated soils. Daytime sensible heat fluxes and orographic mass convergence were considerably reduced, but little triggering was needed for deep convection. In period II deep and localized convection readily developed, usually near solar noon, as shown by the radar and satellite images in Fig. 7. Cumulonimbus over the Rincon Mountains was often observed prior to cumulonimbus over the Catalina Mountains.

Orographic boundary layer dynamics. The surface stations indicate that convergent (anabatic) flow typically started ~1.5 h after sunrise, and peaked before local solar noon, although there was much day-to-day variability (Fig. 8). Both the start and peak times are earlier than expected from the first principles. The average convergence start time was almost the same as the mean start time of the positive surface sensible heat flux (for the same 15 days and 4 ISFF stations, not shown); in other words, anabatic flow started almost immediately following BL heating over the mountain. The first orographic cumuli typically formed shortly after the onset of mass convergence over the mountain (Fig. 8). The magnitude of convergence obtained from flight-level winds on the lowest-level WKA loops was similar to that inferred from the 10 stations around the mountain, although there was considerable day-to-day variability.

An example of the changes in BL properties from pre- to postconvection conditions is illustrated in Fig. 9, showing data from two mountains circumnavigations, separated by ~3 h. The sky was clear at the earlier time, and cumulus congestus billowed over the mountain 3 h later. The average BL θ_e increased somewhat during this time, but its variability became remarkably large (~10 K). This variability is largely due to variations in humidity: the BL on the west
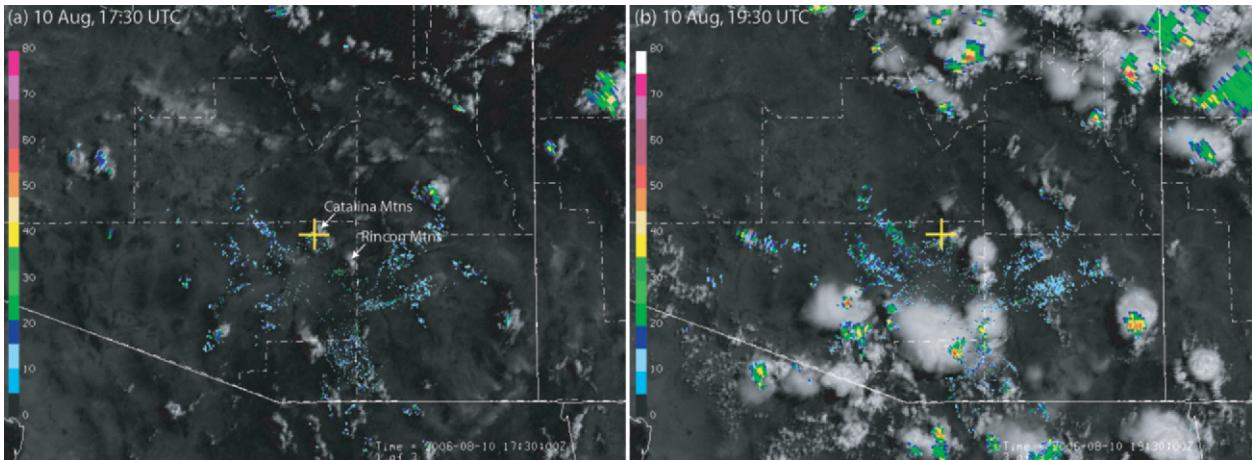
Fɪɢ. 7. Geostationary Operational Environmental Satellite (GOES) visible image overlaid on the KEWX (Tucson) radar reflectivity for 10 Aug 2006 (a) at 1730 UTC and (b) 2 h later, near solar noon. The anvil immediately southeast of Mount Lemmon (yellow cross) in (b) is due to convection over the Rincon Mountains, whose northwestern edge is in the lower-right corner of Fig. 1.
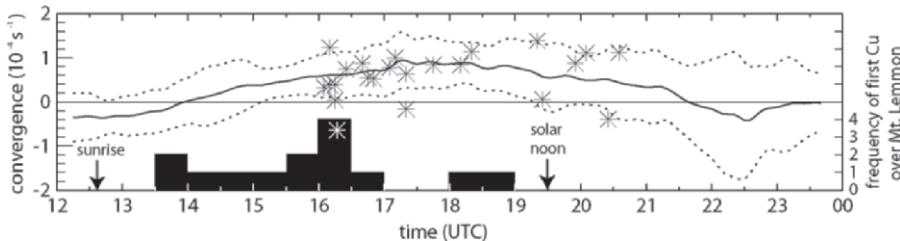

Fɪɢ. 8. Diurnal variation of airmass convergence of 16 flight days listed in Table 1. The solid line is the mean based on 10 ISFF stations (Fig. 1), and the dashed lines are the mean ± one standard deviation. Values derived from 24 aircraft loops at ~310m AGL are shown as stars. The black histogram blocks (labeled on the right) show the range of times of first orographic cumulus appearance over the Catalina Mountains on these 16 days.

convection may occur through column modification by preceding, more shallow convection. Two examples with different modes of modification were seen in IOPs 12 and 15, respectively. We characterize vertical stability by considering profiles of θ_e and the saturated equivalent potential temperature (θ_e^*). The θ_e depends on the temperature and moisture of the air and is conserved for a closed, adiabatic parcel; θ_e^*, which corresponds to a hypothetically saturated atmosphere, depends only on temperature, and is not conserved. Regions where θ_e^* decreases with height are conditionally unstable, and regions where θ_e decreases with height are potentially unstable. The amount of CAPE can be estimated as the vertically integrated positive difference between the BL θ_e and the θ_e^* profile.

Profiles of θ_e and θ_e^* above Windy Point are shown at two times for IOP 12 (Fig. 11). Cumulus congestus was present at 1800 UTC, and a cumulonimbus developed shortly after 1930 UTC. There was an increase in BL θ_e and thus low-level potential instability and CAPE between the two soundings. The BL was shallow at both times with its top at about 3000 m ASL or 1000 m above Windy Point. Above the BL, there was little change in θ_e but a large change in θ_e^*. At 1800 UTC there was a stable layer (increasing θ_e^*)

side was more humid than that on the northeast side, possibly because of differences in natural or man-made soil moisture. Low-level flow convergence was evident at both times, and was stronger at the time cumulus congestus was present (Fig. 9).

The deepening of the BL depth is evident in WCR clear-air echoes presented in Fig. 10. Data from the earlier circumnavigation exhibit weak-echo plumes hardly reaching 1000 m AGL (Figs. 10c,d). The main echo plume captured by the radar during the later circumnavigation was some 2000 m deep and wide, and rose well above the background CBL echoes (Fig. 10h). This plume contained several up- and downdraft cores, yet its flight-level buoyancy (Fig. 10e) was rather small compared to places elsewhere along this and other loops.

Cumulus–environment interaction. One of the fundamental hypotheses of CuPIDO states that deep
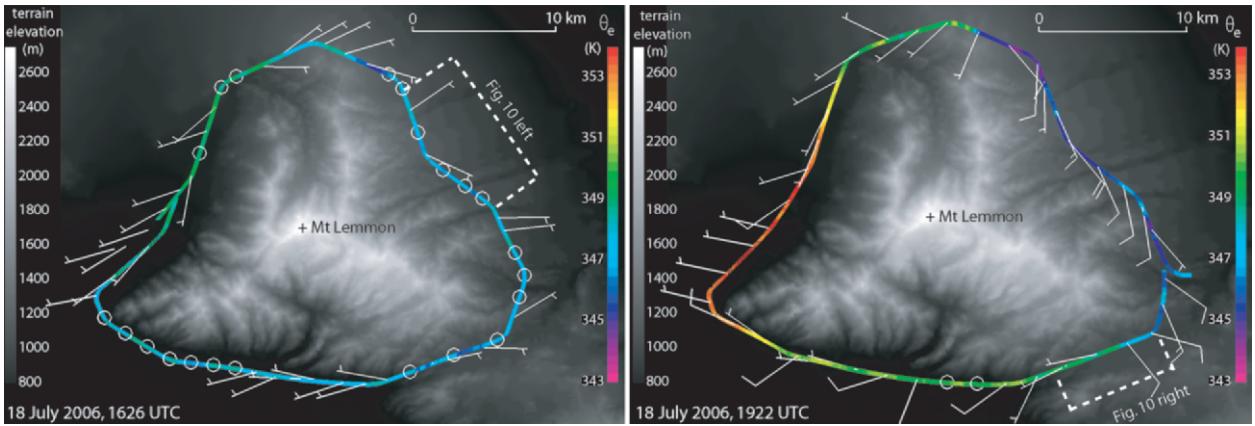
FIG. 9. Flight tracks for two mountain circumnavigations on 18 Jul, the left one before and the right one after the first cumulus congestus formation. The central time of the loops is indicated in the images. The track colors indicate θ_e (K) at flight level, ~310 m AGL; the gray background shows terrain elevation (m). A full wind barb corresponds to 5 m s^{-1}. The white brackets denote the track segments analyzed in Fig. 10.

between 6100 and 7500 m ASL. Between 1800 and 1930 UTC, the cumulus congestus was capped by this layer, and warming occurred beneath 7000 m ASL (detrainment?) and some cooling near 7500 m ASL (ascent forced by the cumuli below?). This resulted in the stable layer being replaced by a conditionally near-neutral atmosphere above 5000 m ASL. Because of the increase in CAPE and the removal of the stable layer, deep convection erupted shortly

after 1930 UTC. In a separate study we will examine whether this behavior of cooling aloft and warming beneath is due to the action of cumulus congestus trapped below the stable layer.

A second example is from IOP 15 (Fig. 12). Three soundings were launched from Mount Lemmon, with cumulus overhead. Thus, they represent the in-cloud or cloud-modified environment. The BL was somewhat drier than during IOP 12, as can be seen by the
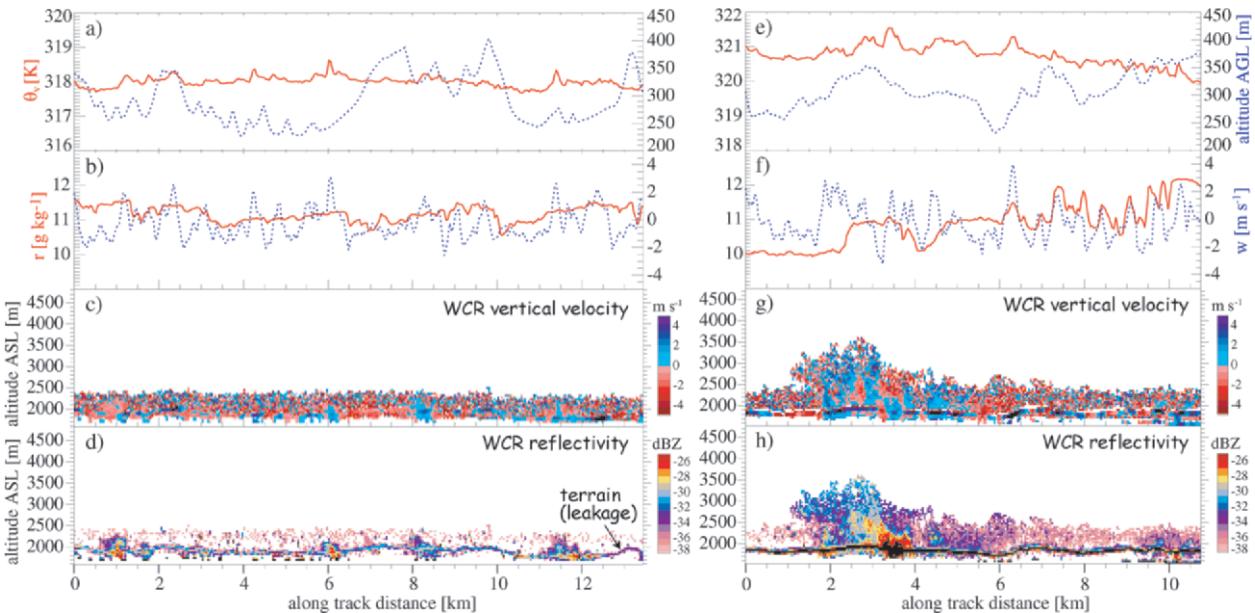

FIG. 10. (top) Flight-level and (c), (g) WCR Doppler and (d), (h) reflectivity data for segments show in Fig. 9 at (left) 1623 and (right) 1914 UTC. (a), (e) Virtual potential temperature (θ_v) and altitude above ground, and (b), (f) water vapor mixing ratio (r) and vertical air velocity (w). The radar is looking up; the strong and thin continuous echo at about 2000 m is a contamination (leaked ground return). The aspect ratio for the WCR panels is 1:1. Note the growth of clear-air plumes in the BL.
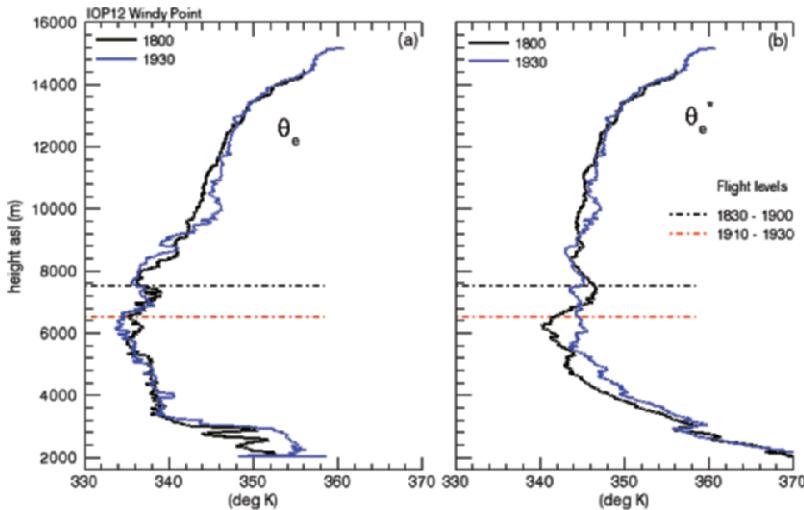
Fig. 11. Profiles of (a) θ_e and (b) θ_e^* for MGAUS launches at 1800 and 1930 UTC from Windy Point on 10 Aug. Windy Point is the southernmost MGAUS launch site in Fig. 1, and was upwind of the orographic cumuli on this day. WKA flight levels at representative times are shown as dash–dot lines. These levels were close to the cumulus tops.
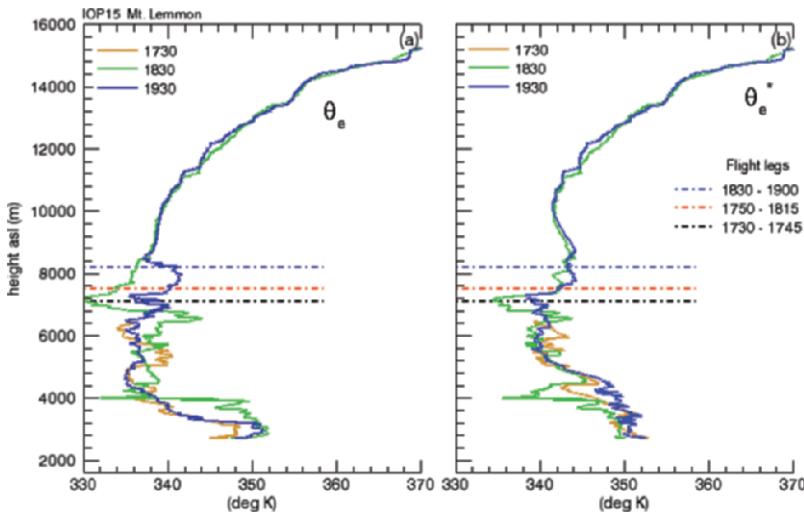

Fig. 12. As Fig. 11, but for MGAUS launches at 1730, 1830, and 1930 UTC from Mount Lemmon on 17 Aug. Note that the UTC sonde failed just above 6000 m. The discontinuities in θ_e and θ_e^* at 4000 and 7000 m ASL at 1830 UTC are most likely due to instrument evaporative cooling as the sonde rose out of cloud (e.g., Wang 2005), as the air was saturated below these levels.

1830, and 1930 UTC, respectively. This is consistent with the notion of successively deeper cumulus modifying the profile by moistening. The weak winds suggest that the deeper clouds develop in the remnants of more shallow cloud columns. However, the BL θ_e increased during this period, as was the case for IOP 12 (Fig. 11), and that alone may explain the observed successive deepening of cumuli. Again, this needs to be examined further.

Cumulus dynamics. Two examples illustrate CuPIDO's potential for the study of fundamental cumulus dynamics. Figure 13 shows typical data collected during aircraft passes near cloud base. The extent of the cloud at 1645 UTC can be inferred from the liquid water content and cloud droplet concentration (top panel); clearly, the echoes penetrated are not clear-air echoes, which are evident at lower levels in Fig. 13c. The most intense updrafts within the cumulus are above flight level—Doppler velocities exceed 9 m s^{-1}, whereas the in situ probe recorded maximum air upward velocities of about 6 m s^{-1}. The intense buoyancy of these young clouds is manifested in the sharp increase in potential temperature (θ). The radar data also captured clear-air echoes; they suggest a link between a plume departing from the downwind side of the peak (visible in the images) and the overlying cloud base. The shape and location of the clear-air plume at 1641 UTC in Fig. 13c, similar to a banner cloud, suggests flow separation in the lee of the peak, with consequent upslope flow from the downwind side and convergence toward the peak (e.g., Schär and Smith 1993). The vertical motion in Fig. 13b suggests circulation.

These observations suggest that a plume model (Turner 1962; Warner 1970) best represents cumulus formation; this must still be verified. Measurements at higher altitudes, and clear visual observations, show

lower values of θ_e in Fig. 12a compared to Fig. 11a. In this case there is very little modification of the θ_e^* (and thus temperature) profile during the IOP. The profile is conditionally neutral or weakly stable above about 6000 m ASL. In contrast, θ_e is being modified. The CBL warms/moistens a little, and it extends, well mixed, up to some 500 m above the mountaintop. More importantly, there is an increase in θ_e with time, with a rising, near-saturated bulge indicated by a local maximum in θ_e at 5000, 7000, and 8000 m at 1730,
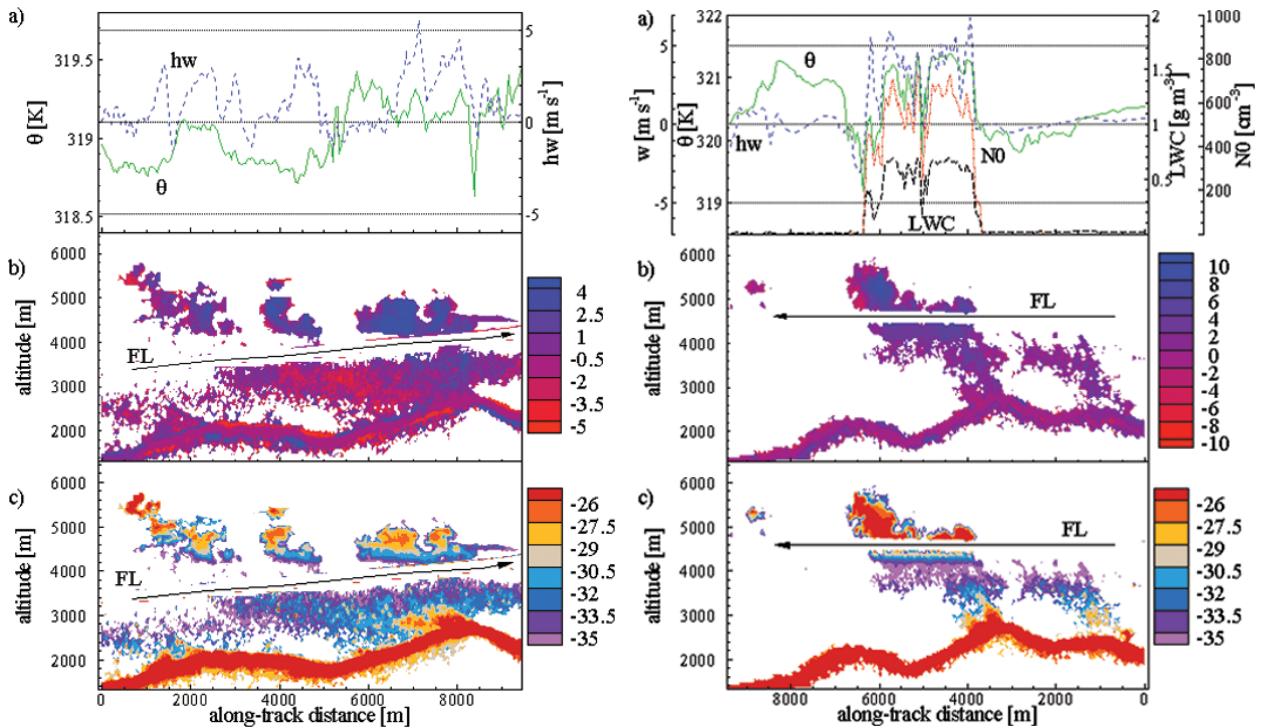
FIG. 13. (a) Flight-level, (b) WCR vertical velocity, and (c) WCR reflectivity data collected during passes near cloud base at (left) 1641 UTC and (right) 1645 UTC 18 Jul. Flight-level data are vertical air velocity (hw), potential temperature (θ), liquid water content (LWC), and cloud droplet concentration (N0). The bold red line in (c) is the terrain. The prevailing wind is from right to left. The clear-air echoes emerging from the mountain are distinct from the cumulus echoes above.

that the turrets evolve as a series of updraft pulses, each of limited extent, more similar to compact thermals. Two vertical pane dual-Doppler (VPDD); (see the "Wyoming Cloud Radar" sidebar) synthe-ses near the tops of two turrets show the internal kinematics (Fig. 14). Clear counterrotating vortex pairs demonstrate the presence of toroidal circulations within the ascending cloud tops (Damiani et al. 2006; Damiani and Vali 2007), similar to those of shedding

thermals (Blyth et al. 1988; Carpenter et al. 1998). These data also suggest dry-air intrusions at the bases of the toroidal thermals. Indications of this behavior also come from our visual observations of how the uppermost ascending volumes of the clouds tend to disconnect from the rest of the turrets below, somewhat pinched by this entertainment mechanism (e.g., Fig. 15). Note how the tops of the turrets show a mushroom appearance, suggesting an undercutting
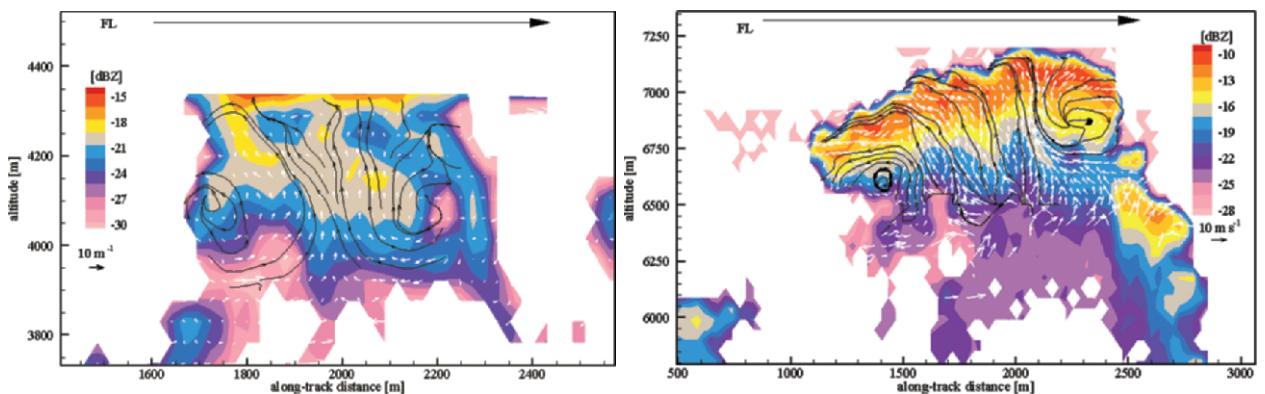

FIG. 14. VPDD analyses of turrets sampled at (left) 1646 and (right) 1751 UTC 10 Aug. Note the mushroom appearance and the intense toroidal circulation with intrusions of presumably dry air (reduced reflectivity) at the bases of the vortices.

FIG. 15. Illustration of turret tops, the left one with a mushroom appearance, and the right one almost detached from the remainder of the cloud below.

of cloudy material resulting from this vertical motion and subsequent entrainment of ambient air. In forthcoming publications, we will complement VPDD and horizontal beam dual-Doppler (HBDD) analyses with Paluch diagrams (Paluch 1979) to interpret the origin and mechanisms of entrainment and detrainment.

SUMMARY. The deployment phase of CuPIDO was highly successful despite some challenges. A number of surface meteorology stations, soundings, and airborne measurements were employed to study moist convection over an isolated mountain. The large array of instruments, focused on a relatively small area, will certainly bring forth new discoveries concerning the interactions between the BL over a mountain, cumulus convection, and the ambient atmosphere, but likely new questions too. The dataset is being used for diagnostic studies of orographic BL flow and cumulus entrainment and detrainment. An unexplored area regards the synergy of stereogrammetrically inferred cloud shell data and radar-inferred cloud interior data. Both datasets are being geolocated in a common grid. We expect this study to yield new insights on cumulus dynamics.

It is easily envisaged that the rich CuPIDO dataset will serve multiple purposes beyond the originally conceived research paths for many years to come. We hope that the CuPIDO dataset will be used by modelers, in particular to study how BL parameterizations affect the timing and intensity of orographic convection. Cloud-resolving models then can be used to improve cumulus parameterizations for continental tropical convection, which is usually calibrated against marine environmental conditions (e.g., Von Salzen and McFarlane 2002).

REFERENCES

Adams, D. K., and A. C. Comrie, 1997: The North American Monsoon. *Bull. Amer. Meteor. Soc.*, **78,** 2197–2213.

Blyth, A. M., and J. Latham, 1993: Development of ice and precipitation in New Mexican summertime cumulus clouds. *Quart. J. Roy. Meteor. Soc.*, **119,** 91–120.

——, W. A. Cooper, and J. B. Jensen, 1988: A study of the source of entrained air in Montana cumuli. *J. Atmos. Sci.*, **45,** 3944–3964.

Braham, R. R., and M. Draginis, 1960: Roots of orographic cumuli. *J. Atmos. Sci.*, **17,** 214–226.

——, S. E. Reynolds, and J. H. Jarrell, 1951: Possibilities for cloud seeding as determined by a study of cloud height versus precipitation. *J. Atmos. Sci.*, **8,** 416–418.

Bryson, R. A., and W. P. Lowry, 1955: Synoptic climatology of the Arizona summer precipitation singularity. *Bull. Amer. Meteor. Soc.*, **36,** 329–339.

Carbone, R. E., J. D. Tuttle, D. A. Ahijevych, and S. B. Trier, 2002: Inferences of predictability associated with warm season precipitation episodes. *J. Atmos. Sci.,* **59,** 2033–2056

Carpenter, R. L., K. K. Droegemeier, and A. M. Blyth, 1998: Entrainment and detrainment in numerically simulated cumulus congestus clouds. Part I: General results. *J. Atmos. Sci.*, **55,** 3417–3432.

Coblentz, D. D., and K. H. Riitters, 2004: Topographic controls on the regional-scale biodiversity of the southwestern USA. *J. Biogeogr.*, **31,** 1125–1138.

Damiani, R., and S. Haimov, 2006: A high-resolution dual-Doppler technique for fixed multi-antenna airborne radar. *IEEE Trans. Geosci. Remote Sens.*, **42,** 3475–3489.

——, and G. Vali, 2007: Evidence for tilted toroidal circulations in cumulus. *J. Atmos. Sci.*, **64,** 2045–2060.

——, ——, and S. Haimov, 2006: The structure of thermals in cumulus from airborne dual-Doppler radar observations. *J. Atmos. Sci.*, **63,** 1432–1450.

Dye, J. E., W. P. Winn, J. J. Jones, and D. W. Breed, 1989: The electrification of New Mexico thunderstorms. Part I. Relationship between precipitation development and the onset of electrification. *J. Geophys. Res.*, **94** (D6), 8643–8656.

Fujita, T., K. A. Styber, and R. A. Brown, 1962: On the mesometeorological field studies near Flagstaff, Arizona. *J. Appl. Meteor.*, **1,** 26–42.

Hales, J. E., 1972: Surges of maritime tropical air northward over the Gulf of California. *Mon. Wea. Rev.*, **100,** 298–306.

——, 1974: Southwestern United States summer monsoon source—Gulf of Mexico or Pacific Ocean? *J. Appl. Meteor.*, **13,** 331–342.

Hobbs, P. V., and A. L. Rangno, 1985: Ice particle concentrations in clouds. *J. Atmos. Sci.*, **42,** 2523–2549.

Leon, D., G. Vali, and M. Lothon, 2006: Dual-Doppler analysis in a single plane from an airborne platform. *J. Atmos. Oceanic Technol.*, **23,** 3–22.

McCollum, D., R. Maddox, and K. Howard, 1995: Case study of a severe mesoscale convective system in central Arizona. *Wea. Forecasting*, **10,** 763–778.

Orville, H. D., 1964: On mountain upslope winds. *J. Atmos. Sci.*, **21,** 622–633.

Paluch, I. R., 1979: The entrainment mechanism in Colorado cumuli. *J. Atmos. Sci.*, **36,** 2467–2478.

Perry, K. D., and P. V. Hobbs, 1996: Influences of isolated cumulus clouds on the humidity of their surroundings. *J. Atmos. Sci.*, **53,** 159–174.

Raymond, D. J., and M. H. Wilkening, 1980: Mountain induced convection under fair weather conditions. *J. Atmos. Sci.*, **37,** 2693–2706.

——, and ——, 1982: Flow and mixing in New Mexico mountain cumuli. *J. Atmos. Sci.*, **39,** 2211–2228.

——, and A. M. Blyth, 1989: Precipitation development in a New Mexico thunderstorm. *Quart. J. Roy. Meteor. Soc.*, **115,** 1397–1423.

Roessner, S., A. I. Flossmann, and H. R. Pruppacher, 1990: The effect on the evolution of the drop spectrum in clouds of the preconditioning of air by successive convective elements. *Quart. J. Roy. Meteor. Soc.*, **116,** 1389–1403.

Schär, C., and R. B. Smith, 1993: Shallow-water flow past isolated topography. Part I. Vorticity production and wake formation. *J. Atmos. Sci.*, **50,** 1373–1400.

Todd, C. J., 1964: Aircraft traverses in a growing mountain cumulus clouds. *J. Atmos. Sci.*, **21,** 529–538.

Turner, J. S., 1962: The "starting plume" in neutral surroundings. *J. Atmos. Sci.*, **13,** 356–368.

Von Salzen, K., and N. A. McFarlane, 2002: Parameterization of the bulk effects of lateral and cloud-top entrainment in transient shallow cumulus clouds. *J. Atmos. Sci.*, **59,** 1405–1430.

Wang, J., 2005: Evaluation of the dropsonde humidity sensor using data from DYCOMS-II and IHOP_2002. *J. Atmos. Oceanic Technol.*, **22,** 247–257.

Warner, J., 1970: On steady-state-one-dimensional models of cumulus convection. *J. Atmos. Sci.*, **27,** 1035–1040.

Zehnder, J. A., L. Zhang, D. Hansford, A. Radzan, N. Selover, and C. M. Brown, 2006: Using digital cloud photogrammetry to characterize the onset and transition from shallow to deep convection over orography. *Mon. Wea. Rev.*, **134,** 2527–2546.

——, J. Hu, and A. Razdan, 2007: A stereo photogrammetric technique applied to orographic convection. *Mon. Wea. Rev.*, **135,** 2265–2277.